DUAL-FREQUENCY SIMULATIONS OF RADAR OBSERVATIONS OF TORNADOES

David J. Bodine[1,2,3,*], Robert D. Palmer[2,3], Takashi Maruyama[4], Caleb J. Fulton[3,5], and Boon Leng Cheong[3,5]

[1] Advanced Study Program, National Center for Atmospheric Research, Boulder, CO, USA
[2] School of Meteorology, University of Oklahoma, Norman, OK, USA
[3] Advanced Radar Research Center, University of Oklahoma, Norman, OK, USA
[4] Disaster Prevention Research Institute, Kyoto University, Kyoto, Japan
[5] School of Electrical and Computer Engineering, University of Oklahoma, Norman, OK, USA

1. INTRODUCTION

Radars measure reflectivity-weighted particle velocities rather than air velocities, resulting in measurement errors when Doppler velocities are used to estimate tornado wind speeds. Snow (1984) and Dowell et al. (2005) show that debris is centrifuged outward relative to the air, and the radial difference between air and particle velocities (u_r) depends on vortex dynamics and particle characteristics. Moreover, Dowell et al. (2005) also showed that the tangential and vertical velocities of debris are reduced relative to the air speed. In their simulations, they showed that differences between air and particle velocities can reach tens of m s^{-1} for larger scatterers. Finally, Doppler velocity measurements for a single scatterer type represent a mass-weighted average, and thus portions of the resolution volume with higher debris concentrations have a greater contribution to Doppler velocity measurements (Lewellen et al. 2008).

Because large differences between air and particle velocities occur in tornadoes, these measurement errors must be corrected in Doppler velocity measurements to obtain accurate wind velocities. Given strong scientific interest in understanding near-surface wind speeds (e.g., to assess societal impacts or understand corner flow structure), mitigating debris centrifuging errors close to the ground remains a critical yet elusive goal because large debris exhibits the highest concentrations near the surface (e.g., Wurman et al. 1996; Wurman and Gill 2000; Dowell et al. 2005), thus leading to the largest differences between air and particle velocities. Errors in Doppler velocity due to debris centrifuging also hinder our understanding of three-dimensional wind speeds in tornadoes. Nolan (2013) showed that vertical velocities retrieved from single-Doppler analyses are significantly biased due to debris centrifuging effects and inadequate low-level sampling of tornadic inflow layers. In particular, they showed that anomalously strong retrieved downdrafts result from increased radial divergence caused by debris centrifuging.

To address the debris centrifuging bias problem, Wakimoto et al. (2012) propose a technique to correct debris centrifuging bias by assuming the scatterers in the tornado are rain drops, and then calculating a median diameter based on radar reflectivity factor. A limitation to this technique is that the dominant scatterers must be rain drops or small objects with similar electromagnetic and aerodynamic characteristics, otherwise the correction is underestimated. Polarimetric radar observations frequently reveal areas of low co-polar cross-correlation coefficient (ρ_{HV}) at S (Ryzhkov et al. 2005; Kumjian and Ryzhkov 2008; Bodine et al. 2013), C (Palmer et al. 2011; Schultz et al. 2012a,b), and X bands (Bluestein et al. 2007; Snyder and Bluestein 2014), even in rural areas where perhaps larger scatterers are less common. These observations suggest that dominant scatterers exhibit Mie scattering (i.e., D $> \frac{\lambda}{16}$) at these frequencies, thus suggesting that the Rayleigh assumption does not apply in such cases. Thus, the rain drop scattering assumption requires further testing, and new methods are needed to correct debris centrifuging effects for larger scatterers.

In the present study, idealized experiments are performed to simulate radar observations of tornadoes at multiple frequencies using a Large-Eddy Simulation (LES) model and T-matrix calculations. Simulations are conducted to examine differences in equivalent reflectivity factor and Doppler velocity over common weather radar frequencies, and these simulations reveal significant frequency dependence of these radar variables. Based on these simulations, recommendations for estimating and mitigating velocity errors associated with debris centrifuging and extracting information about debris characteristics are presented.

2. RADAR VARIABLE SIMULATIONS USING THE LES MODEL

In this section, the LES model used to generate the tornado-like flow and calculate particle trajectories is discussed. Then, methods used to simulate equivalent reflectivity factor and Doppler velocity at different radar frequencies are presented.

The LES model simulates the flow of a vortex chamber (Davies-Jones 1973; Church et al. 1979), producing a wide range of tornado-like flows. The reader is referred to Maruyama (2011) and Bodine (2014) for more details about the numerical calculation scheme of the LES model. The vortex flow in the present study is a two-cell vortex with

* *Corresponding author address:* David Bodine, NCAR, 3450 Mitchell Lane, Boulder, CO 80302; e-mail: dbodine@ucar.edu

a maximum mean tangential wind speed of 58 m s^{-1} at a radius of 253 m. Mean axisymmetric radial, tangential and vertical velocities are shown in Figure 1(a) – (c). Axisymmetric averaging causes a slight positive vertical velocity in the vortex core at the surface because the vortex center meanders.

Debris trajectories are computed using three-dimensional wind fields from the LES model as described in Maruyama (2011) and Bodine (2014). The trajectory calculation employs second-order Runge-Kutta integration and allows the drag force coefficient to vary as a function of the particle Reynolds number for spherical particles (applied herein for rain drops). For wood particles, a constant drag force coefficient of 2 is employed for a square plate (Simiu and Scanlan 1996), such as a plywood sheet. Trajectory calculations were tested in Bodine (2014), and results similar to Dowell et al. (2005) were obtained for radial, tangential and vertical velocities for idealized vortices.

Two scatterer types are simulated in the present study: rain drops and wood objects. Rain drop trajectories are computed for the following diameters: 0.5, 1, 1.5, 2, and 4 mm. For each drop size, 100,000 trajectories are calculated to provide a sufficient number of trajectories for stable particle concentration and velocity statistics. However, due to computational constraints, it is not feasible to explicitly simulate all trajectories required for a drop-size distribution (DSD) with a high number concentration (e.g., hundreds or thousands of drops per m^3). Thus, we employ a scaling factor, S_i, so that each drop represents S_i drops. Accordingly, a much larger number of drops can be simulated in the domain as long as accurate statistics for debris concentration and velocity are obtained. The scaling factors used for each drop size are presented in Table 1. The scaling factors are weighted by a Marshall-Palmer distribution (Marshall and Palmer 1948) with a rain rate of 20 mm hr^{-1}. For wood objects, 10000 wood board trajectories are computed for ten different sizes with radii of 9.5 – 95 mm.

T-matrix calculations (Waterman 1969, 1971) are performed to obtain backscatter amplitudes and calculate equivalent reflectivity factor, Z_e. To encompass all frequency bands used in radar studies of tornadoes, T-matrix calculations are performed at S, C, X, Ka, and W bands. The complex relative permittivity for rain drops are based on Ray (1972), and the complex relative permittivities of wood objects are obtained from Daian et al. (2006) and Jebbor et al. (2011). Unfortunately, complex relative permittivities for wood objects have only been measured at S and X bands, and thus some uncertainty exists in their applicability at other wavelengths. A comprehensive investigation of complex relative permittivities of common debris is needed to improve electromagnetic scattering calculations for debris.

Table 1: Drop diameters and scaling factors, S_i, used to compute equivalent reflectivity factor and Doppler velocity. The total number of drops in the simulation domain is the scaling factor multiplied by the number of trajectories. The scaling factor is weighted by a Marshall-Palmer drop-size distribution with a rain rate of 20 mm hr^{-1}.

Drop diameter (mm)	Low Conc. S_i	High Conc. S_i
0.5	3.36×10^4	3.36×10^6
1	5.38×10^3	5.38×10^5
1.5	1.84×10^3	1.84×10^5
2	8.51×10^2	8.51×10^4
4	59.2	5.92×10^3

T-matrix calculations have limitations when used to simulate radar measurements of debris. First, debris may be non-spherical, high aspect ratio, and can have high refractive indices. T-matrix calculations cannot capture the scattering effects caused by irregularities in shape, and T-matrix calculations may not converge for particles with large eccentricity or high refractive indices. Thus, T-matrix calculations for debris are limited to a subset of possible scatterer types in tornadoes. Even with these limitations, T-matrix calculations seem to capture basic scattering properties of tornadic debris. For the 10 May 2010 Moore-Oklahoma City, Oklahoma tornado, Bodine et al. (2014) found that T-matrix-derived equivalent reflectivity factor for debris exhibits similar characteristics to statistical properties of the debris field (e.g., large dual-wavelength Z_{HH} differences).

In the present study, particles are simulated over a large range of particle sizes and frequencies, so spherical particles are used in the T-matrix calculations to enable convergence. Thus, it is assumed that the mean Z_e for a high aspect ratio spheroid over all orientations is similar to the Z_e of an equivalent-volume sphere. To test this assumption, mean Z_e over all orientations for a spheroid with an aspect ratio of $\frac{1}{7}$ is compared to Z_e for a sphere at S, C, and X bands. At these frequencies, differences between Z_e for the randomly oriented spheroid and sphere are 0.8, 1.1, and 0.4 dB, respectively, when averaged over the size range for wood objects. Given the small differences in Z_e, it is assumed that small differences also occur at Ka and W bands. It is worth noting that shape effects may be significant in some cases, and are especially important for polarimetric radar variables. However, the present discussion focuses only on Z_e and Doppler velocity.

Equivalent reflectivity factors for wood debris and rain drops are shown in Figures 2 and 3 for common weather radar

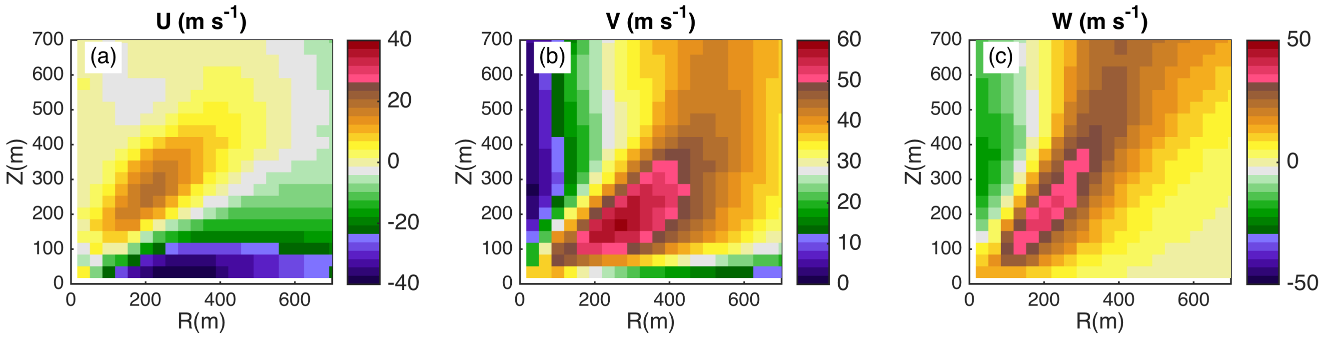

Figure 1: Radial, tangential and vertical velocities (m s^{-1}) from the LES model (a) – (c). The maximum inflow velocity is 39 m s^{-1}, and the maximum tangential velocity is 58 m s^{-1}.

frequencies. Large dual-wavelength Z_e differences, often called dual-wavelength ratios (DWR) or dual-frequency ratios (DFR), are evident for all frequency pairs. S-C band and S-X band DFRs are on the order of 10 and 20 dB, respectively, which are similar to DFRs observed for hail (e.g., Atlas and Ludlam 1961; Snyder et al. 2010; Picca and Ryzhkov 2012), and debris (Bodine et al. 2014). At cm-wavelengths, Mie scattering effects are prominent with complex variations in Z_e for small variations in particle size. However, a general trend of increasing Z_e is evident at all frequencies shown with an increase of about 20 dB as particle size increases from a diameter of 20 to 200 mm. At Ka band, as wood board diameters exceed 40 mm, oscillations caused by Mie scattering diminish and Z_e follows the optical scattering approximation. Similar behavior is observed at W band except the optical scattering region encompasses smaller wood board diameters as well.

Mean Doppler velocity, $\overline{v}(r_0)$, is a mean value of individual scatterers' velocities, $v_p(r_1)$, weighted by their radar reflectivities, $\eta(r_1)$, and illumination functions (Doviak and Zrnić 1993), as follows:

$$\overline{v}(r_o) = \frac{\int\int\int v_p(r_1)\eta(r_1)I(r_0,r_1)dV_1}{\int\int\int \eta(r_1)I(r_0,r_1)dV_1} \tag{1}$$

The illumination function weights the scatterers' backscatter cross sections (e.g., due to the antenna or range weighting function). Based on (1), it is evident that scatterers with large reflectivities or high number concentrations will have a greater impact on Doppler velocity measurements.

Radar variables are computed for LES data axisymmetrically averaged to a radial and vertical grid spacing of 33.7 m. Using these axisymmetric means, mean equivalent reflectivity factor Z_e and mean reflectivity-weighted velocity are calculated using T-matrix calculations for the experiments discussed in Table 1. Mean reflectivity-weighted velocity is used to approximate Doppler velocity, and this approximation generates good results if scatterers are uniformally distributed throughout the resolution volume and are present in relatively high concentrations. Hereafter, mean reflectivity-weighted radial and tangential velocities are referred to as u_{dr} and v_{dr}. The radial and tangential velocity measurement errors, associated with assuming the radar measures air velocity, are u_{dr} - U and v_{dr} - V, respectively. Future studies could employ a realistic radar simulator (e.g., Cheong et al. 2008, 2014) to examine how radar resolution volume size, attenuation, sidelobes, non-uniform debris distributions, etc., affect radar measurements in tornadoes at different frequencies.

Dual-frequency velocity differences will also be examined, and may provide information about Doppler velocity errors. Radial and tangential dual-frequency velocity differences will be computed, DDU and DDV, respectively, and represent the velocity difference measured by an idealized dual-frequency radar (i.e., matched beam radar system). *Radial* dual-frequency velocity differences (DDU) correspond to simulated dual-frequency velocity differences where the radar beam aligns with radial particle motion (e.g., an range-height indicator scan through the vortex center). Mathematically, this is represented as follows:

$$DDU = u_{dr}(f_2) - u_{dr}(f_1), \tag{2}$$

where f_1 and f_2 are the two radar frequencies. Likewise, DDV is computed as shown in (3), and represents the simulated dual-frequency velocity difference where the radar beam aligns with tangential particle motion.

$$DDV = v_{dr}(f_2) - v_{dr}(f_1) \tag{3}$$

In a different application, dual-frequency velocity differences have been applied to sizing of ice crystals (Matrosov 2011). Differential velocity has also been computed in tornadoes using (single-frequency) polarimetric radars by taking a velocity difference between the horizontal and vertical polarizations (Snyder and Bluestein 2014).

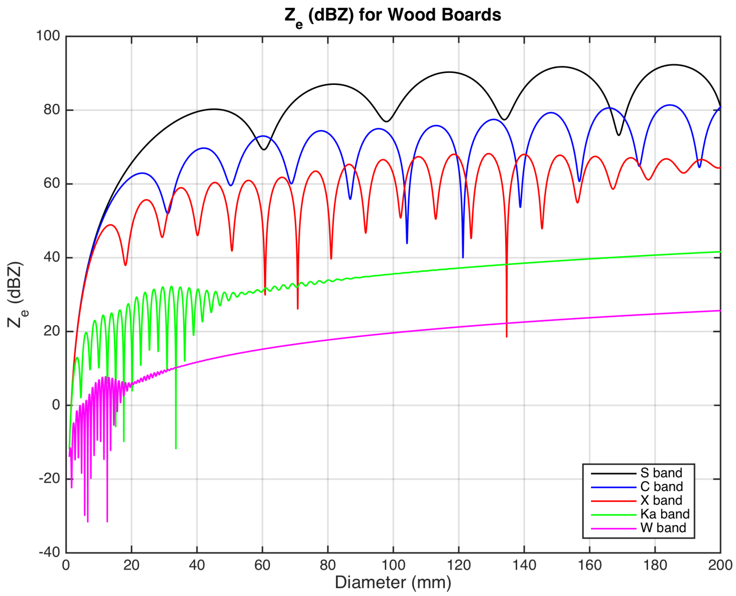

Figure 2: Plot of equivalent reflectivity factor (Z_e, dBZ) for wood objects at S, C, X, Ka, and W bands. Z_e varies by approximately 60 dB between S and W bands for a concentration of 1 m^{-3}.

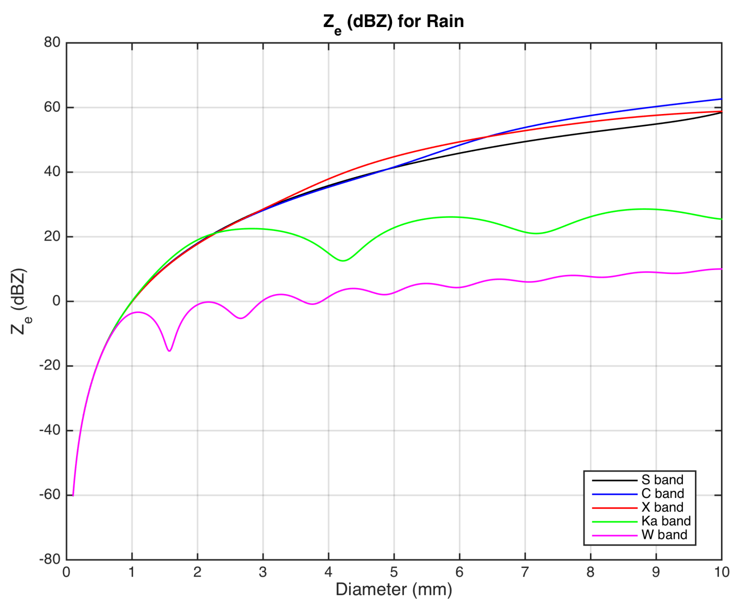

Figure 3: Plot of equivalent reflectivity factor (Z_e, dBZ) for rain drops at S, C, X, Ka, and W bands for a concentration of 1 m^{-3}. For large rain drops, dual-frequency differences can approach 40 dB for the largest expected drop sizes (e.g., about 8-mm diameters).

Table 2: Equivalent reflectivity factor and mean Doppler velocity for the simplified example with a 1000-m^3 resolution volume containing 10 wood objects with a mean equivalent diameter of 130 mm, and rain drops.

Radar frequency band	Wood objects Z_e (dBZ)	Rain drops Z_e (dBZ)	Doppler velocity (m s^{-1})
S	68.4	40.9	40.0
C	55.2	40.8	40.3
X	44.1	40.9	42.3
Ka	17.6	42.0	47.0
W	0.6	23.1	47.5

3. SIMULATIONS OF FREQUENCY DEPENDENCE OF RADAR MEASUREMENTS IN TORNADOES

In this section, radar simulations of equivalent reflectivity factor and Doppler velocity are presented at multiple frequencies. Relationships between physical properties of the scatterers (e.g., size) and dual-frequency radar variables are also examined.

3.1. Idealized case study

To illustrate the impact of transmit frequency on Doppler velocity measurements in tornadoes, consider the following simplified example with a 1000-m^3 resolution volume. In this resolution volume, 10 wood objects are simulated with diameters uniformally distributed between 110 – 150 mm, producing a Z_e of 68.4 dBZ at S band (Table 2). The maximum S-band equivalent reflectivity factor observed in tornadic debris signatures (TDSs; Ryzhkov et al. 2002, 2005) is approximately 70 dBZ (Bunkers and Baxter 2011; Bodine et al. 2013), thus suggesting number concentrations lower than 1 m^{-3} (Figure 2). The resolution volume also contains 3360 0.5-mm and 184 2-mm diameter drops m^{-3} (the drops are scaled in the same manner as Table 1), producing an S-band Z_e of 40.9 dBZ. In this example, a simple geometry is assumed such that scatterer motion, wind direction, and the radar beam are aligned. To simulate differences between air and radar-measured wind speeds, in this example, the wind speed is 50 m s^{-1}, the wood board velocity is 40 m s^{-1}, and the 0.5-mm and 2-mm diameter drops' velocities are 49 and 47 m s^{-1}. The slower velocities of the larger particles replicate the slower tangential velocities of larger particles compared to the air velocity.

Simulated equivalent reflectivity factor and Doppler velocity for the example resolution volume are shown in Table 2. Equivalent reflectivity factor exhibits large variations across common weather radar frequencies as a consequence of Mie scattering, consistent with Figure 2. In contrast, rain drops are predominately in the Rayleigh scattering region for cm-wavelengths, and thus dual-wavelength differences are small. Rain drops are in the Mie scattering region at W band, resulting in lower equivalent reflectivity factor.

The large range of wood board Z_e for different frequencies produces an important effect on which dominant scatterer type and thus Doppler velocity. At S and C bands, equivalent reflectivity factor for wood objects is tens of dB greater than rain drops, and consequently, simulated S- or C-band Doppler velocity are within 0.3 m s^{-1} of the wood objects' velocities. However, at Ka and W bands, rain drops produce an equivalent reflectivity factor that exceeds the wood objects by 22 – 24 dB. As a result, the measured Doppler velocities are very close to the velocity of the large drops (which contribute more to equivalent reflectivity factor than the small drops in this case). At X band, equivalent reflectivity factor contributions from wood objects and rain drops are closer; however, the wood objects still have slightly higher Z_e and thus a greater effect on Doppler velocity.

The strong dependence of Doppler velocity on transmit frequency results from Mie scattering effects and the size distribution of particles. Mie scattering effects can be understood in the context of the backscatter cross-section. For Rayleigh scatterers, the backscatter cross-section (σ_b) is

$$\sigma_b = \frac{\pi^5}{\lambda^4} |K_m|^2 D^6, \tag{4}$$

where $|K_m|$ is a function of the scatterer's refractive index and D is the scatterer's diameter (Doviak and Zrnić 1993). From (4), it is apparent that the backscatter cross-section could vary by several orders of magnitude over the common weather radar frequencies (e.g., 3-mm to 10-cm) because of the λ^4 dependence. For example, the backscatter cross-sections of a 1-mm diameter rain drop at S and W bands are 2.84 $\times$ 10^{-6} and 1.1 mm^2, respectively. In contrast, backscatter cross-sections for wood objects exhibit small differences among frequencies in the Mie scattering region with differences primarily resulting from oscillations caused by constructive and destructive interference. For example, the backscatter cross-sections of a 100-mm diameter wood board at S and W bands are 160 and 239 mm^2, respectively. Equivalent reflectivity factor can be computed from backscatter cross-sections as follows:

$$Z_e = \frac{\lambda^4}{\pi^5 |K_w|^2} \int_0^\infty \sigma_b(D) N(D) dD, \tag{5}$$

where $N(D)$ is the particle size distribution. For Rayleigh scatterers, it is apparent that the λ^4 dependence in (4) is removed for Z_e in (5). However, for scatterers with similar backscatter cross-sections at different frequencies (e.g., wood objects), the λ^4 dependence causes much higher equivalent reflectivity factor at lower frequencies (longer wavelengths), as illustrated in Figure 2.

Because the rain drop concentrations are several orders of magnitude larger than debris concentration (e.g., 10^3 m^{-3} compared to 0.01 m^{-3}), the frequency differences in backscatter cross-section have a significant impact. At W band, the backscatter cross-section of a wood board exceeds the 1-mm rain drop by a factor of 100 whereas the rain drop concentration exceeds the wood board concentration by a factor of 10^5. As a result, rain drops are the dominant scatterers when computing reflectivity. However, at S band, the backscatter cross-section of the rain drop is very small, and thus the wood objects dominate the backscattered radar signal.

3.2. Doppler velocity simulations

In this section, simulations of equivalent reflectivity factor and Doppler velocity are performed using a LES model and T-matrix calculations. Simulations are conducted for common weather radar frequencies from S to W bands.

To assess the effects of large and small particles, concentrations are varied based on observed TDS characteristics. Debris simulations are conducted for low and high debris concentrations (LD and HD, respectively), and for low and high rain drop concentrations (LR and HR, see Table 1). For the HD experiments, 1000 debris trajectories are computed for each wood board size (i.e., uniform size distribution). In the LD concentration experiments, mean equivalent reflectivity factor is scaled by a factor of 1/100 rather than reducing the number of trajectories to maintain stable three-dimensional statistics of particle velocity and concentrations.

The first experiment simulates a tornado with a high debris, and high rain drop concentration (HDHR). Simulated Z_e for wood objects, rain drops, and all particles are shown in Figure 4 for S, X, and W bands. Similar to the idealized example, S-band Z_e is dominated by debris except where debris concentrations are very small (Figure 4a – c). In contrast, even large concentrations of debris have little effect on W-band Z_e (Figure 4g – i), which is evident by very small differences between simulated Z_e for rain and all particles. At X-band, rain and debris are dominant scatterers in different regions of the simulated tornado, resulting in a more complex spatial pattern of Z_e (Figure 4d – f). Within the volume enclosed by r $<$ 200 m and z $<$ 100 m, Z_e exhibits larger contributions from debris.

S-band reflectivity-weighted velocities deviate significantly from air velocities as a consequence of the greater contributions of debris to Z_e. Radial and tangential reflectivity-weighted particle velocities are shown in Figure 5a,b, and the difference between radial and tangential reflectivity-weighted particle velocities and air velocities (i.e., measurement error associated with air and Doppler velocity differences) are shown in Figure 5c,d. Comparing u_{dr} and v_{dr} to LES model velocities (Figure 1), a significant reduction in S-band inflow layer depth and maximum inflow velocities occurs, and tangential velocities are reduced within the radius of maximum wind. Maximum radial velocity differences exceed 25 m s^{-1} and occur where wood objects are the dominant scatterers (Figure 5h). A secondary v_{dr} maximum occurs in the corner flow region between radii of 300 – 400 m where debris with higher tangential velocities fall into the low tangential velocity corner flow, producing a maximum in tangential velocity error.

Dual-frequency velocity differences provide useful information about the spatial structure and magnitudes of Doppler velocity errors associated with differences between air and reflectivity-weighted particle velocities. Dual-frequency velocity differences between reflectivity-weighted S and W band radial and tangential velocities are shown in Figure 5e,f. Assuming differences in the illumination function are small (e.g., a matched beam dual-frequency radar), these reflectivity-weighted velocity differences correspond to velocity differences between an S and W band radar system. Radial and tangential velocity errors exhibit good correlation with dual-frequency velocity difference measurements (DDU and DDV), with correlation coefficients of 0.98 and 0.90, respectively. Moreover, dual-frequency velocity differences have a root-mean squared error of 2.1 and 2.5 m s^{-1} for radial and tangential velocity errors, respectively.

Significant differences between reflectivity-weighted velocities and air velocities occur at X-band as well (Figure 6). Wood objects remain the dominant scatterers in the lowest 100 m. Inflow layer and maximum inflow velocities are reduced, although not as significantly as the S band case. Maximum magnitudes of radial and tangential velocity errors are 19.1 and 15.6 m s^{-1}, respectively (Figure 6c,d). Radial and tangential dual-frequency X-W band velocity differences exhibit strong correlation, with correlation coefficients of 0.96 and 0.91, respectively. Root-mean squared errors for both radial and tangential velocity differences remain small (1.9 and 2.0 m s^{-1}, respectively).

Dual-frequency equivalent reflectivity factor differences may provide useful information about debris size. S-W band dual-frequency Z_e differences are shown in Figure 5g. S-W band dual-frequency Z_e differences exhibit strong correlation (0.92) with dominant scatterer radius (Figure 5h). Dual-frequency X-W equivalent reflectivity factor differences exhibit a weaker correlation (0.74) to debris size (Figure 6). S-W band dual-frequency Z_e exhibits a stronger correlation because scatterers at S band remain in the Rayleigh scattering region for a larger diameter range compared to X band. Thus, dual-frequency Z_e differences increase as a function of particle size over a larger diameter range.

In contrast to the cm-wavelengths, small differences between reflectivity-weighted velocities and air velocities occur at W band (Figure 7). Radial and tangential reflectivity-weighted velocities exhibit close agreement to model wind fields,

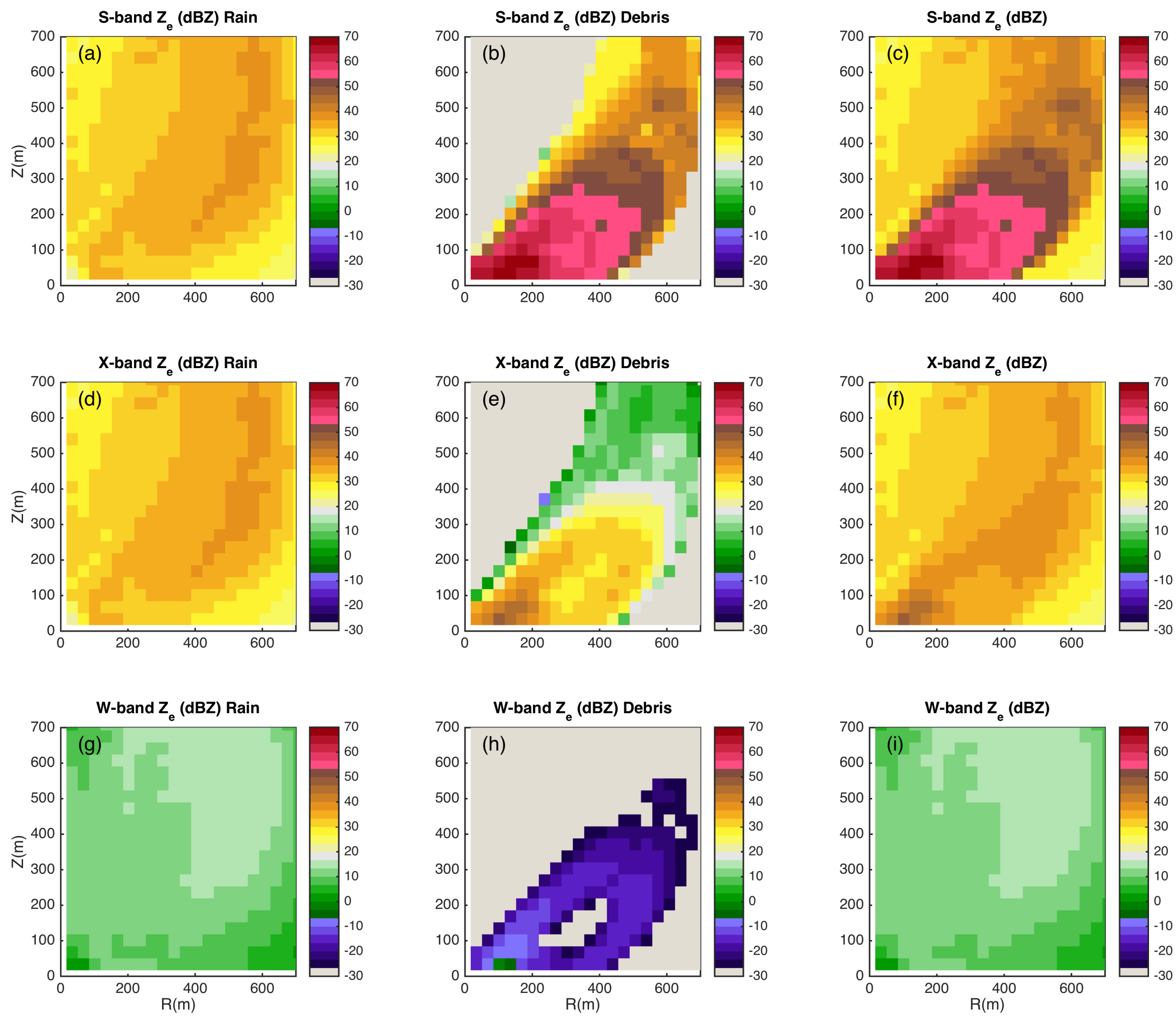

Figure 4: Z_e (dBZ) for rain, debris and all particles at S band (a) – (c), X band (d) – (f), and W band (g) – (i) for the high debris, high rain drop concentration (HDHR) experiment. Dominant scatterer types change significantly depending on radar frequency. At S band, dominant scatterer types are primarily debris except where debris concentrations are very small. At W band, rain drops are the dominant scatterers throughout the simulation domain. At X band, dominant scatterer type varies throughout the domain, although debris has greater contributions to Z_e within the near-surface flow of the tornado.

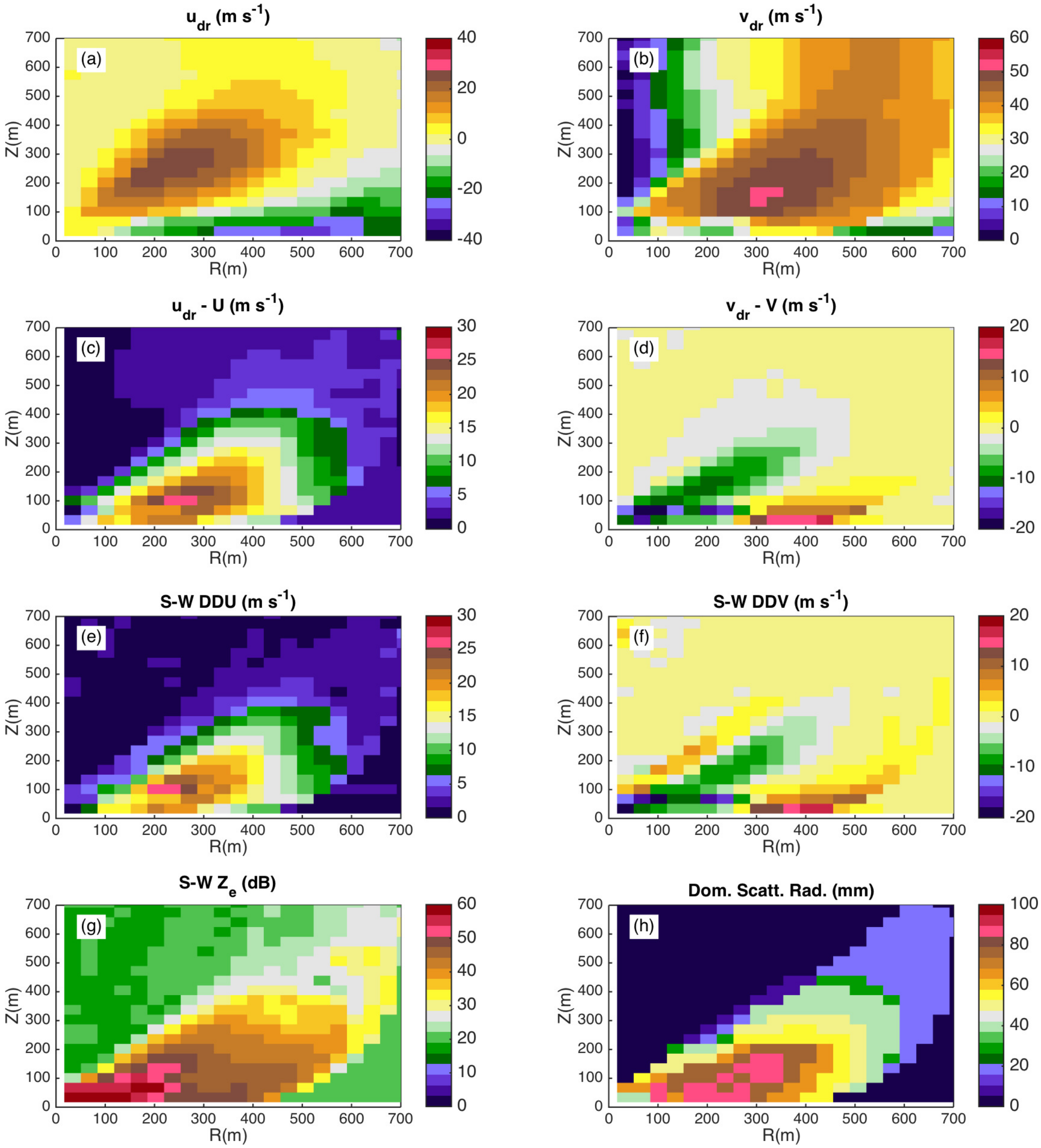

Figure 5: S-band reflectivity-weighted radial (a) and tangential (b) velocities, S-band radial (c) and tangential (d) difference between reflectivity-weighted particle and air velocities, radial (e) and tangential (f) dual-frequency (S-W) velocity differences, S-W Z_e difference (g), and S-band dominant scatterer radius (h).

Table 3: Statistics for simulated mean radial velocity error (m s^{-1}) in the lowest 300 m at S, C, X, Ka, and W bands for the four experiments. Because of the scaling factor, the results from the HDHR and LDLR simulations are the same.

Experiment	HDLR	HDHR	LDLR	LDHR
S band	9.3	9.0	9.0	6.6
C band	9.1	8.3	8.3	4.1
X band	8.8	5.6	5.6	3.3
Ka band	5.0	2.4	2.4	2.3
W band	2.7	1.7	1.7	1.7

and the depth and peak inflow velocities are well-resolved. The dominant scatterers are rain drops, resulting in small magnitudes of radial and tangential velocity errors, generally less than 5 m s^{-1}. Considering that the HDHR experiment simulates the highest expected debris concentrations in TDSs (e.g., S-band Z_e approaching 70 dBZ), W-band velocity measurements are shown to be quite robust to debris centrifuging errors even in an extreme case.

Mean radial velocity error (u_{dr} - U) within the lowest 300 m for the four experiments is shown in Table 3. The HDHR and LDLR experiments are the same because the scaling factors reduce Z_e for rain and debris by the same factor. The LDLR illustrates that a small concentration of debris could cause significant velocity errors if rain drops or other small scatterers are not present in high concentrations. The HDLR experiments shows a "worst-case scenario" for velocity measurement errors with high concentrations of wood objects and low concentrations of rain drops. For all scenarios, mean W-band velocity errors are small (less than 3 m s^{-1}). Not surprisingly, at S band, significant velocity errors occur for each scenario. For the frequencies in between S and W bands, velocity errors decrease as rain concentrations increase and/or debris concentrations decrease.

4. DEBRIS CENTRIFUGING ERROR DETECTION AND MITIGATION

Because debris centrifuging can cause significant errors in Doppler velocity, methods to correct such errors are needed. While simulations herein suggest that mm-wavelength radars may mitigate velocity errors even when concentrations of rain drops (or other small particles) are low and debris concentrations are high, attenuation effects may limit the utility of mm-wavelength radars when rain drop or debris concentrations are very high. Moreover, fixed cm-wavelength radars have been vital to observing many high impact tornado events (e.g., Burgess et al. 2002; Palmer et al. 2011; Schultz et al. 2012a,b; Atkins et al. 2014), and have been used extensively to simultaneously document storm-scale and tornado-scale evolution (e.g., Bluestein et al. 2007; Wurman et al. 2007a,b; French et al. 2008; Tanamachi et al. 2012). Thus, debris centrifuging corrections for cm-wavelength radars remain an important goal.

Co-polar cross-correlation coefficient (ρ_{hv}) provides an opportunity to assess contributions of Rayleigh and Mie scattering at cm-wavelengths (e.g., testing the Rayleigh scattering assumption used in the Wakimoto et al. (2012) correction method). If rain drops are the dominant scatterers (or other small Rayleigh scattering particles), ρ_{hv} values should be close to unity. Schwarz and Burgess (2011) and Bodine et al. (2011) noted TDS cases in which ρ_{hv} increased during periods of suspected precipitation entrainment, although in these cases ρ_{hv} remained below expected values for rain. A cursory polarimetric radar time series experiment by Bodine et al. (2011) showed a relationship between increasing ρ_{hv} and increasing Z_{HH} contribution from rain, suggesting that ρ_{hv} may provide an indicator of the relative contributions of Rayleigh and Mie scatterers. A more comprehensive study is needed to investigate the relationship between ρ_{hv} and the relative contributions of rain drops and debris.

Dual-frequency radars, or collocated radars with different transmit frequencies, have significant potential for estimating debris centrifuging errors on Doppler velocity measurements. Dual-frequency variables, such as dual-frequency ratio or attenuation may help characterize spatial distributions of debris size or concentrations. To develop corrections for cm-wavelengths, comparisons between dual-frequency velocity differences and polarimetric radar variables available from a single-frequency, polarimetric radar may enable robust corrections for velocity errors. ρ_{hv}, differential velocity (Snyder and Bluestein 2014), spectral polarimetric densities radar variables, etc., in particular, may exhibit relationships to debris characteristics.

5. CONCLUSIONS

Simulations are conducted to better understand the effects of transmit frequency on radar observations of tornadoes. Significant dual-frequency differences occur for equivalent reflectivity factor and Doppler velocity, particularly as the frequency difference increases. Such differences arise due to Mie scattering and the reduction in Z_e for large particles at higher frequencies, which reduce their overall contribution to Z_e while contributions of small particles (close to or within the Rayleigh scattering region) remain high because of their large concentrations. Experiments are

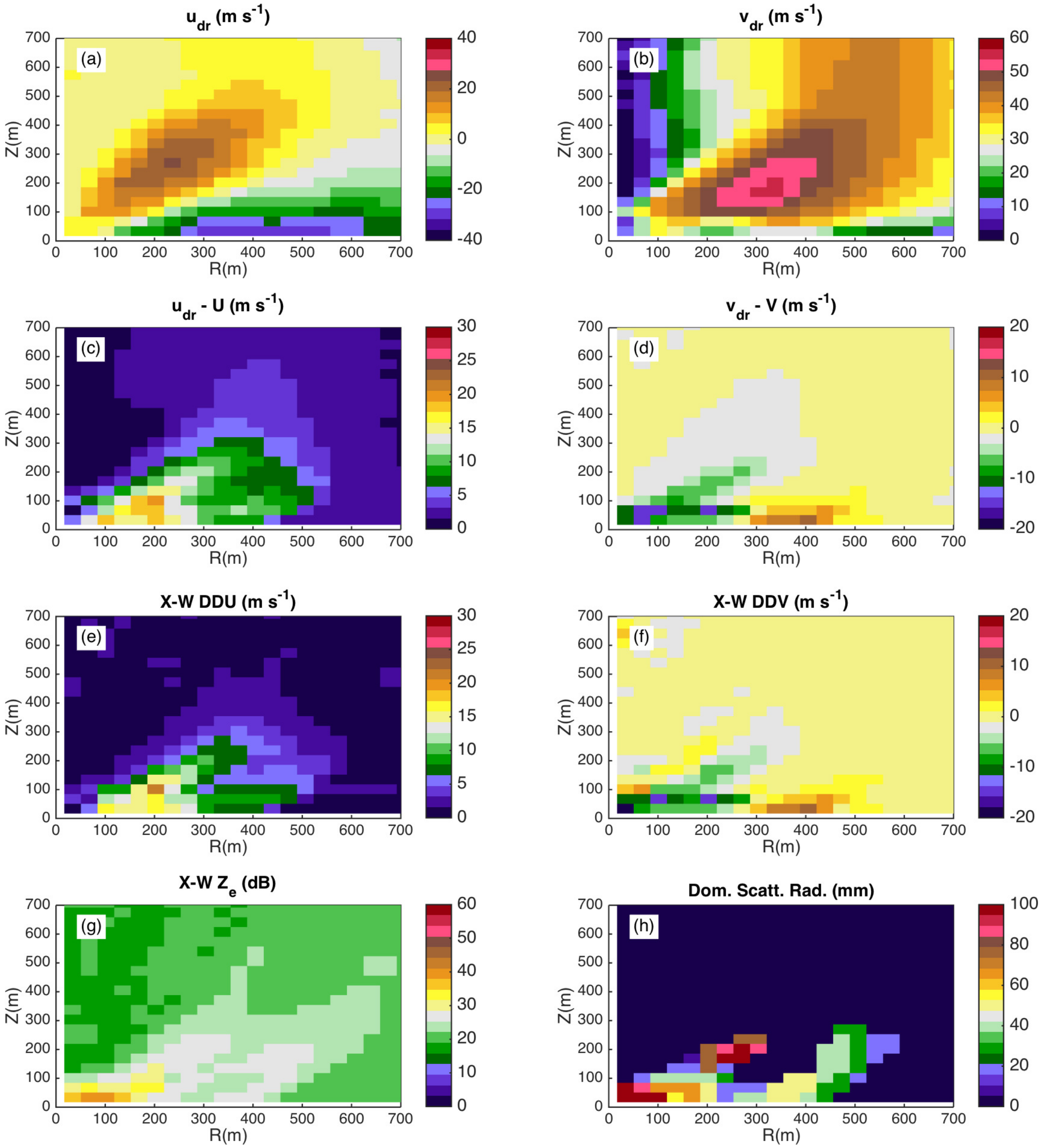

Figure 6: X-band reflectivity-weighted radial (a) and tangential (b) velocities, X-band radial (c) and tangential (d) difference between reflectivity-weighted particle and air velocities, radial (e) and tangential (f) dual-frequency (X-W) velocity differences, X-W Z_e difference (g), and X-band dominant scatterer radius (h).

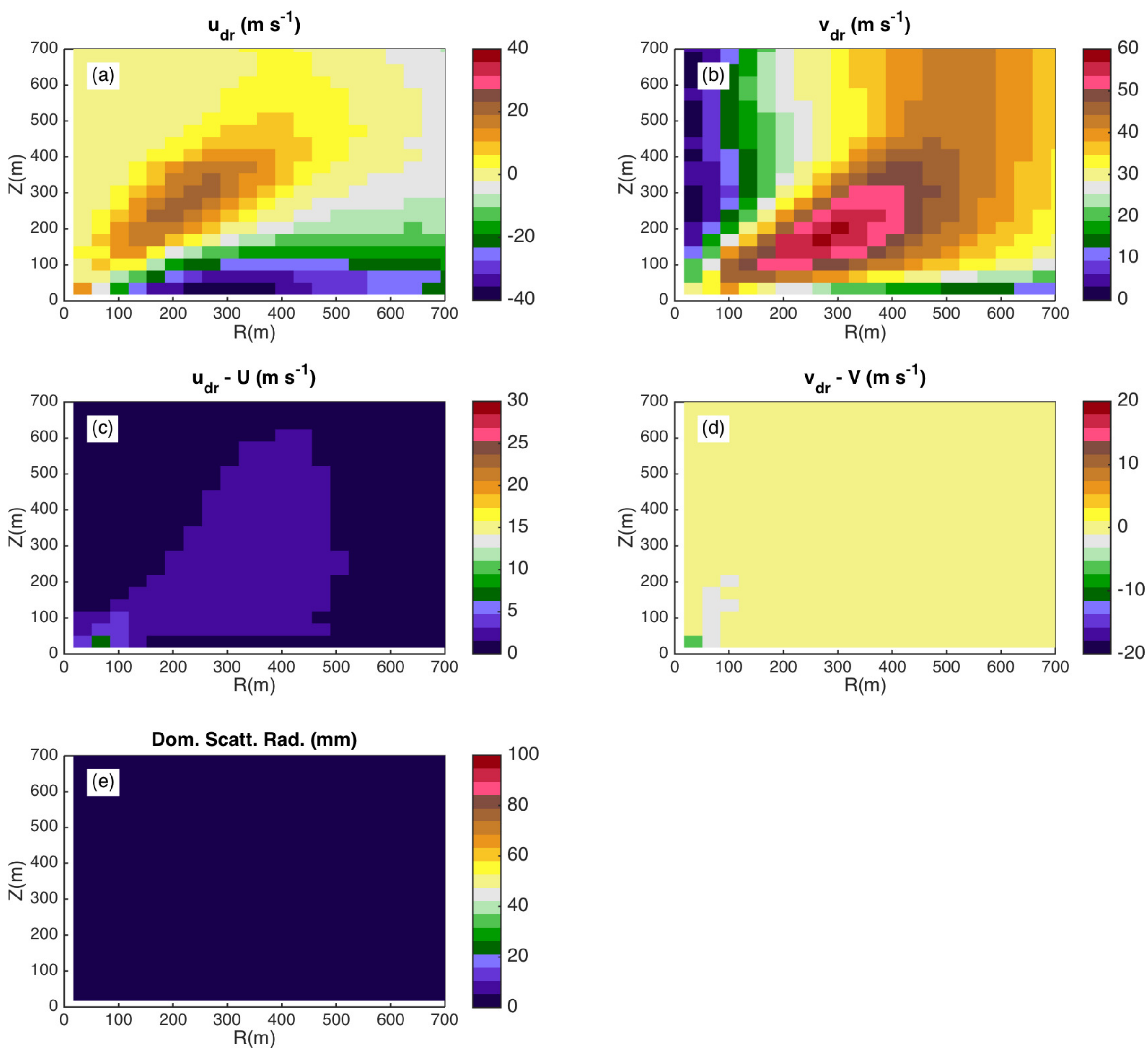

Figure 7: W-band reflectivity-weighted radial (a) and tangential (b) velocities, W-band radial (c) and tangential (d) difference between reflectivity-weighted particle and air velocities, and W-band dominant scatterer radius (e).

conducted for four scenarios involving low and high debris concentrations, and low and high rain drop concentrations.

The simulations of equivalent reflectivity factor and Doppler velocity reveal that determining the dominant scatterers in tornadoes is a complex process. Dominant scatterers are highly dependent on the transmit frequency and electromagnetic scattering characteristics of particles illuminated by the radar. Interestingly, at W band, rain drops are the dominant scatterers for all of the experiments conducted herein, even with large wood board concentrations that produce equivalent reflectivity factor at S band of 70 dBZ (i.e., among the highest values expected based on previous TDS studies). At S band, however, wood objects are dominant scatterers, even in low concentrations, resulting in significant errors in simulated Doppler velocity measurements. At X band, dominant scatterer type exhibits greater spatial variability depending on the concentration of rain drops and debris. For cases with low concentrations of rain drops or high concentrations of debris, wood objects dominate equivalent reflectivity factor and Doppler velocity in the near-surface region containing the highest debris concentrations. However, in the low debris concentration, high rain drop concentration case, rain drops are the dominant scatterers throughout.

Dual-frequency variables are discussed as a potential avenue for determining particle size and estimating Doppler velocity errors associated with using reflectivity-weighted particle velocities to measure air velocity. Dual-frequency Z_e shows a general correlation with particle size where wood objects are present. Dual-frequency velocity differences using a pairing of W band with a lower frequency also exhibit close agreement with Doppler velocity errors, and exhibit small root-mean squared errors (less than 1.5 m s^{-1}) when used as an estimator for the Doppler velocity error.

The simulations herein suggest that the assumption by Wakimoto et al. (2012) applies very well at W band (and generally Ka band) because rain drops are the dominant scatterers even with high debris concentrations. Because the upper portion of the drop-size distribution is in the Mie scattering region for mm-wavelengths, a T-matrix based approach could be used to compute relationships between radar reflectivity factor and mean size, and used to apply Wakimoto et al. (2012)'s correction method. On the other hand, cm-wavelength simulations reveal that dominant scatterer type may vary spatially in the tornado vortex, and suggest that small particles are not the dominant scatterers at low altitudes unless the concentration of large particles is small. Hence, it is suggested that debris-centrifuging correction techniques involving Rayleigh scattering assumptions be considered conservative corrections at cm-wavelengths unless evidence of Rayleigh scattering is observed (e.g., high ρ_{hv} or small dual-wavelength Z_e differences). Additional methods are needed to improve debris centrifuging error estimates in non-Rayleigh scattering cases. Such methods could involve a two-step approach where non-Rayleigh scatterers are identified and correction methods are applied there first, and then the method of Wakimoto et al. (2012) could be applied to areas where Rayleigh scattering applies.

Dominant scatterers for mm-wavelength radars are found to be rain drops or similarly small particles in high concentrations (e.g., sand or soil particles). Even in the absence of rain, tornadoes likely ingest much higher concentrations of small particles. This assumption could be tested through a concerted effort to collect dual-/multiple frequency radar data with collocated mobile radars or through the development of dual-frequency mobile radar systems. Such radar studies, coupled with detailed video/photography tornadoes and associated debris fields, would be instrumental in understanding and correcting debris centrifuging errors on Doppler velocity.

Debris electromagnetic scattering characteristics are poorly understood due to their complexity and large variety of shapes, sizes, and compositions, yet Doppler radar measurements in tornadoes are strongly dependent upon the electromagnetic scattering characteristics of debris. To address this need, a research project is on-going to better understand debris electromagnetic scattering characteristics and polarimetric TDSs. To ascertain electromagnetic scattering characteristics of different debris types, advanced numerical techniques are being employed such as Ansys HFSS or High Frequency Simulation Software and are being compared to radar cross section measurements made in anechoic chambers at the Advanced Radar Research Center at the University of Oklahoma.

Using the radar cross section data, polarimetric TDSs will be simulated using a polarimetric radar time-series simulator (Cheong et al. 2014). To obtain a realistic wind field, the radar simulator uses high-resolution model wind fields (including, but not limited to, the LES model herein), and trajectories can be computed for a large range of particle types, sizes, and concentrations. Such efforts will provide a much improved understanding of the effects of different debris types on TDSs and Doppler velocity, and should enable improved methods to characterize debris distributions and correct debris centrifuging errors.

6. ACKNOWLEDGMENTS

This study is based upon work supported by the National Science Foundation under Grants No. AGS-1303685 and OISE-1209444. The first author is supported by the National Center for Atmospheric Research (NCAR) Advanced Study Program. NCAR is sponsored by the National Science Foundation. The authors thank Tammy Weckwerth for comments on a draft of this paper.

References

Atkins, N. T., K. M. Butler, K. R. Flynn, and R. M. Wakimoto, 2014: An integrated damage, visual, and radar analysis of the 2013 Moore Oklahoma EF5 tornado. *Bull. Amer. Meteor. Soc., in press*.

Atlas, D. and F. H. Ludlam, 1961: Multi-wavelength radar reflectivity of hailstorms. *Quart. J. Roy. Meteor. Soc.*, **87**, 523–534.

Bluestein, H. B., M. M. French, R. L. Tanamachi, S. Frasier, K. Hardwick, F. Junyent, and A. Pazmany, 2007: Close-range observations of tornadoes in supercells made with a dual-polarization, X-band, mobile Doppler radar. *Mon. Wea. Rev.*, **135**, 1522–1543.

Bodine, D., 2014: *Polarimetric radar observations and numerical simulations of tornadic debris*. Ph.D. thesis, University of Oklahoma.

Bodine, D., M. R. Kumjian, R. D. Palmer, P. L. Heinselman, and A. V. Ryzhkov, 2013: Tornado damage estimation using polarimetric radar. *Wea. Forecasting*, **28**, 139–158.

Bodine, D., M. R. Kumjian, A. J. Smith, R. D. Palmer, A. V. Ryzhkov, and P. L. Heinselman, 2011: High-resolution polarimetric observations of an EF-4 tornado on 10 May 2010 from OU-PRIME. *35th Conf. on Radar Meteorology*, Amer. Meteor. Soc., 3B.4.

Bodine, D. J., R. D. Palmer, and G. Zhang, 2014: Dual-wavelength polarimetric radar analyses of tornadic debris signatures. *J. Appl. Meteor. Climatol.*, **53**, 242–261.

Bunkers, M. J. and M. A. Baxter, 2011: Radar tornadic debris signatures on 27 April 2011. *Electronic J. Operational Meteor.*, **12**, 1–6.

Burgess, D. W., M. A. Magsig, J. Wurman, D. C. Dowell, and Y. Richardson, 2002: Radar observations of the 3 May 1999 Oklahoma City tornado. *Wea. Forecasting*, **17**, 456–471.

Cheong, B. L., D. Bodine, T. Maruyama, C. Fulton, S. Torres, and R. D. Palmer, 2014: A radar-cross-section database driven radar time-series simulator. *8th European Conf. on Radar*.

Cheong, B. L., R. D. Palmer, and M. Xue, 2008: A time series weather radar simulator based on high-resolution atmospheric models. *J. Atmos. Oceanic Technol.*, **25**, 230–243.

Church, C. R., J. T. Snow, G. L. Baker, and E. M. Agee, 1979: Characteristics of tornado-like vortices as a function of swirl ratio: A laboratory investigation. *J. Atmos. Sci.*, **36**, 1755–1776.

Daian, G., A. Taube, A. Birnboim, M. Daian, and Y. Shramkov, 2006: Modeling the dielectric properties of wood. *Wood Sci. Technol.*, **40**, 237–246.

Davies-Jones, R. P., 1973: The dependence of core radius on swirl ratio in a tornado simulator. *J. Atmos. Sci.*, **30**, 1427–1430.

Doviak, R. J. and D. S. Zrnić, 1993: *Doppler Radar and Weather Observations*. Dover Publications, Mineola, New York, 2nd edition.

Dowell, D. C., C. R. Alexander, J. M. Wurman, and L. J. Wicker, 2005: Centrifuging of hydrometeors and debris in tornadoes: Radar-reflectivity patterns and wind-measurement errors. *Mon. Wea. Rev.*, **133**, 1501–1524.

French, M. M., H. B. Bluestein, D. C. Dowell, L. J. Wicker, M. R. Kramar, and A. L. Pazmany, 2008: High-resolution, mobile Doppler radar observations of cyclic mesocyclogenesis in a supercell. *Mon. Wea. Rev.*, **136**, 4997–5016.

Jebbor, N., S. Bri, A. Nakheli, L. Bejjit, M. Hdddad, and A. Mamouni, 2011: Complex permittivity determination with the transmission/reflection method. *Int. J. Emerg. Sci.*, **4**, 682–695.

Kumjian, M. R. and A. V. Ryzhkov, 2008: Polarimetric signatures in supercell thunderstorms. *J. Appl. Meteor. Climatol.*, **48**, 1940–1961.

Lewellen, D. C., B. Gong, and W. S. Lewellen, 2008: Effects of finescale debris on near-surface tornado dynamics. *J. Atmos. Sci.*, **65**, 3247–3262.

Marshall, J. S. and W. M. K. Palmer, 1948: The distribution of raindrops with size. *J. Meteor.*, **5**, 165–166.

Maruyama, T., 2011: Simulation of flying debris using a numerically generated tornado-like vortex. *J. Wind Eng. Ind. Aerodynamics*, **99**, 249–256.

Matrosov, S. Y., 2011: Feasibility of using radar differential Doppler velocity and dual-frequency ratio for sizing particles in thick ice clouds. *J. Geophys. Res.*, **116**, 1–13.

Nolan, D. S., 2013: On the use of Doppler radar-derived wind fields to diagnose the secondary circulations of tornadoes. *J. Atmos. Sci.*, **70**, 1160–1171.

Palmer, R. D., D. Bodine, M. Kumjian, B. Cheong, G. Zhang, Q. Cao, H. B. Bluestein, A. Ryzhkov, T.-Y. Yu, and Y. Wang, 2011: The 10 May 2010 tornado outbreak in central Oklahoma: Potential for new science with high-resolution polarimetric radar. *Bull. Amer. Meteor. Soc.*, **92**, 871–891.

Picca, J. and A. Ryzhkov, 2012: A dual-wavelength polarimetric analysis of the 16 May 2010 Oklahoma City extreme hailstorm. *Mon. Wea. Rev.*, **140**, 1385–1403.

Ray, P. S., 1972: Broadband complex refractive indices of ice and water. *Appl. Optics*, **11**, 1836–1844.

Ryzhkov, A., D. Burgess, D. Zrnić, T. Smith, and S. Giangrande, 2002: Polarimetric analysis of a 3 May 1999 tornado. *Preprints, 21th Conf. on Severe Local Storms*, Amer. Meteor. Soc., ed., San Antonio, TX.

Ryzhkov, A. V., T. J. Schuur, D. W. Burgess, and D. S. Zrnić, 2005: Polarimetric tornado detection. *J. Appl. Meteor.*, **44**, 557–570.

Schultz, C. J., L. D. Carey, E. V. Schultz, B. C. Carcione, C. B. Darden, C. C. Crowe, P. N. Gatlin, D. J. Nadler, W. A. Petersen, and K. R. Knupp, 2012a: Dual-polarization tornadic debris signatures Part I: Examples and utility in an operational setting. *Electronic J. Operational Meteor.*, **13**, 120 – 137.

Schultz, C. J., S. E. Nelson, L. D. Carey, L. Belanger, B. C. Carcione, C. B. Darden, T. Johnstone, A. L. Molthan, G. J. Jedlovec, E. V. Schultz, C. C. Crowe, and K. R. Knupp, 2012b: Dual-polarization tornadic debris signatures Part II: Comparisons and caveats. *Electronic J. Operational Meteor.*, **13**, 138–158.

Schwarz, C. M. and D. W. Burgess, 2011: Supercell polarimetric signatures at X-band: Data from VORTEX2. *35th Conf. on Radar Meteorology*, Amer. Meteor. Soc., ed., 7B.4.

Simiu, E. and R. H. Scanlan, 1996: *Wind effects on structures: Fundamentals and applications to design*. John Wiley, 688 pp., 3rd edition.

Snow, J. T., 1984: On the formation of particle sheaths in columnar vortices. *J. Atmos. Sci.*, **41**, 2477–2491.

Snyder, J. C. and H. B. Bluestein, 2014: Some considerations for the use of high-resolution mobile radar data in tornado intensity determination. *Wea. Forecasting*, **29**, 799 – 827.

Snyder, J. C., H. B. Bluestein, G. Zhang, and S. J. Frasier, 2010: Attenuation correction and hydrometeor classification of high-resolution, X-band, dual-polarized mobile radar measurements in severe convective storms. *J. Atmos. Oceanic Technol.*, **27**, 1979–2001.

Tanamachi, R. L., H. B. Bluestein, J. B. Houser, S. J. Frasier, and K. M. Hardwick, 2012: Mobile X-band, polarimetric Doppler radar observations of the 4 May 2007 Greensburg, Kansas, tornadic supercell. *Mon. Wea. Rev.*, **140**, 2103–2125.

Wakimoto, R. M., P. Stauffer, W. C. Lee, N. T. Atkins, and J. Wurman, 2012: Finescale structure of the LaGrange, Wyoming tornado during VORTEX2: GBVTD and photogrammetric analyses. *Mon. Wea. Rev.*, **140**, 3397–3418.

Waterman, P. C., 1969: Scattering by dielectric obstacles. *Alta Frequenza*, **(Speciale)**, 348–352.

— 1971: Symmetry, unitarity and geometry in electromagnetic scattering. *Phys. Rev. D*, **3**, 825 – 839.

Wurman, J. and S. Gill, 2000: Fine-scale radar observations of the Dimmitt, Texas (2 June 1995), tornado. *Mon. Wea. Rev.*, **128**, 2135–2164.

Wurman, J., Y. Richardson, C. Alexander, S. Weygandt, and P.-F. Zhang, 2007a: Dual-doppler analysis of winds and vorticity budget terms near a tornado. *Mon. Wea. Rev.*, **135**, 2392–2405.

— 2007b: Dual-doppler and single-doppler analysis of a tornadic storm undergoing mergers and repeated tornadogenesis. *Mon. Wea. Rev.*, **135**, 736–758.

Wurman, J., J. M. Straka, and E. N. Rasmussen, 1996: Fine-scale Doppler radar observations of tornadoes. *Science*, **272**, 1774–1777.